sustainability

MDPI

Article

Tri-*tert*-butyl(*n*-alkyl)phosphonium Ionic Liquids: Structure, Properties and Application as Hybrid Catalyst Nanomaterials

Daria M. Arkhipova [1,2,*], Vadim V. Ermolaev [2], Vasili A. Miluykov [2], Farida G. Valeeva [2], Gulnara A. Gaynanova [2], Lucia Ya. Zakharova [2], Mikhail E. Minyaev [1] and Valentine P. Ananikov [1]

[1] N.D. Zelinsky Institute of Organic Chemistry, Russian Academy of Sciences, Leninsky Prospect, 47, 119991 Moscow, Russia; mminyaev@ioc.ac.ru (M.E.M.); val@ioc.ac.ru (V.P.A.)
[2] Arbuzov Institute of Organic and Physical Chemistry, FRC Kazan Scientific Center, Russian Academy of Sciences, Arbuzov Str. 8, 420088 Kazan, Russia; ermolaev@iopc.ru (V.V.E.); miluykov@iopc.ru (V.A.M.); valeevaf@iopc.ru (F.G.V.); ggulnara@bk.ru (G.A.G.); lucia@iopc.ru (L.Y.Z.)
* Correspondence: arkhipova_daria@ioc.ac.ru

Abstract: A series of sterically hindered tri-*tert*-butyl(*n*-alkyl)phosphonium salts (*n*-C_nH_{2n+1} with n = 1, 3, 5, 7, 9, 11, 13, 15, 17) was synthesized and systematically studied by ^{1}H, ^{13}C, ^{31}P NMR spectroscopy, ESI-MS, single-crystal X-ray diffraction analysis and melting point measurement. Formation and stabilization palladium nanoparticles (PdNPs) were used to characterize the phosphonium ionic liquid (PIL) nanoscale interaction ability. The colloidal Pd in the PIL systems was described with TEM and DLS analyses and applied in the Suzuki cross-coupling reaction. The PILs were proven to be suitable stabilizers of PdNPs possessing high catalytic activity. The tri-*tert*-butyl(*n*-alkyl)phosphonium salts showed a complex nonlinear correlation of the structure–property relationship. The synthesized family of PILs has a broad variety of structural features, including hydrophobic and hydrophilic structures that are entirely expressed in the diversity of their properties

Keywords: sterically hindered phosphonium ionic liquids; PdNPs; TEM; Suzuki cross-coupling reaction; DLS

Citation: Arkhipova, D.M.; Ermolaev, V.V.; Miluykov, V.A.; Valeeva, F.G.; Gaynanova, G.A.; Zakharova, L.Y.; Minyaev, M.E.; Ananikov, V.P. Tri-*tert*-butyl(*n*-alkyl)phosphonium Ionic Liquids: Structure, Properties and Application as Hybrid Catalyst Nanomaterials. *Sustainability* **2021**, *13*, 9862. https://doi.org/10.3390/su13179862

Academic Editor: Paula Ossowicz

Received: 28 July 2021
Accepted: 31 August 2021
Published: 2 September 2021

1. Introduction

Ionic liquids (ILs) are typically composed of an organic cation (ammonium, imidazolium, phosphonium, pyridinium, sulfonium) and inorganic anion [1]. These compounds are of much interest due to the combination of attractive properties such as limited volatility and flammability, broad temperature range of the liquid state, thermal and chemical stability, wide electrochemical potential window, tunable solubility and miscibility and highly variable biological activity [2–6]. The main feature of ILs is a high variability of the structure (more than 10^6 possible compounds), which gives unprecedented opportunities for customization for specific tasks.

The first members of IL as a class attributed to the reports the synthesis of ethanolammonium nitrate by Gabriel [7] at the end of the 19th century and ethylammonium nitrate by Walden [8] at the beginning of the 20th century. The discovery of moisture- and air-stable ionic liquids in the 1990s resulted in an increased number of publications devoted to ILs—Scopus showed >13,000 publications in this field at the end of 2018 [9,10]. At the same time, Morton and Hamer noted a decrease in the number of patent claims related to the synthesis of new ILs. The main trend for now is developing their industrial application [11].

One of the promising fields of IL application is energy storage devices [12], as electrolytes in Li-ion batteries [13], including IL-modified polymers [14]. Considering a number of requirements for the electrolyte, ILs are often the system of choice for these purposes [15]. Currently, sodium-ion batteries are under intensive development [16], and ILs have been proposed to be used as electrolytes in such devices [17]. The IL application in electrochemistry extends to the modification of electrodes [18] and design of supercapacitors [19].

Illustrating the use of ILs is their employment in biomedicine [20] and related areas [21]. The range of their activity is not limited only by antimicrobial ability [22]; ILs also exhibit antitumor [23] and antiviral activity [24]. In biotechnology, ILs serve as an effective solvent for pre-extraction treatment [25] and cellulose dissolution [26]. In tribology, ILs became useful as a lubricant [27] and continued to develop in this direction [28,29].

In general, the role of a tunable solvent for various chemical processes is the main area of application for ILs [30,31]. One of the most remarkable contributions of ILs in the chemical industry is observed in the field of transition metal catalysis [2,32]. In the case of nanosized catalysts, ILs serve as both stabilizers and solvents [33–35]. To enhance catalysis efficiency, the rational design of ILs should be emphasized [36].

The microstructure [37] and ecotoxicity of ILs [38,39] are emerging topics of much attention. The conjunction of hydrogen bonding and ionic interactions of the IL forces microstructural directionality. Such a supramolecular network acts as an "entropic driver" for the design of complex multiscale frames [40].

MacFarlane defines the development prospective of IL study [41]. Electrochemistry and biotechnology are highlighted as the most promising fields of IL adaptation in the industry.

The IL capabilities for tuning allow the achievement of specific microstructures and distinct macroscopic functions [37]. Based on the above, ILs are in high demand and require comprehensive study of the novel members of this unique family of compounds [42]. This trend is currently realized in systematic studies of IL lines [43,44]. Particular attention has been paid to phosphonium ionic liquids (PILs) due to their thermal stability. Resistance to decomposition under basic conditions is of special note comparing to nitrogen-containing analogues [45,46]. PILs have found their application in solving urgent problems such as the separation of platinum group metals from used automotive catalysts [47], in fuel desulfurization [48], CO_2 sorption [49] and energy storage [50].

In our group, the first examples of sterically hindered PILs were synthesized and described [51]. Earlier we have demonstrated that steric hindrance of PILs plays a key role in nanoparticle stabilization and their catalytic activity in Suzuki cross-coupling reaction. This effect is similar to the catalysis by Pd complexes with sterically demanded phosphines, although the mechanism of the processes is definitely different [52,53]. Previously, we have synthesized and investigated sterically hindered PILs with even numbers of carbon atoms in side chain [54]. Here, we systematically extended the series of sterically hindered PILs with compounds containing odd numbers of methylene fragments in alkyl substituents and characterized them. The obtained PILs were applied to design a catalytic system based on PdNPs. The catalytic hybrid material was characterized with TEM and DLS and successfully tested in Suzuki cross-coupling reaction.

2. Materials and Methods

2.1. Instruments

NMR spectroscopy. NMR spectra were recorded on a Fourier 300 HD instrument (Bruker, Fällanden, Switzerland) at 21 °C (^{1}H 300.13 MHz, ^{31}C 75.47 MHz) and AVneo 300 instrument (Bruker, Fällanden, Switzerland) at 21 °C (^{31}P 121.54 MHz). $SiMe_4$ was used as an internal reference for ^{1}H and ^{13}C NMR spectra, and 85% H_3PO_4 was used as an external reference for ^{31}P NMR spectra.

Single-crystal X-ray diffraction analysis. X-ray diffraction data for **2b** and **3b** (Table 1) were collected at 100 K on a Quest D8 diffractometer (Bruker, Bremen, Germany) equipped with a Photon-III area-detector (shutterless φ- and ω-scan technique), using monochromatized Mo K_α-radiation. The intensity data were integrated by the SAINT program [55] and corrected for absorption and decay using SADABS [56].

The X-ray diffraction data for **4b** were recollected at 100 K on a four-circle Synergy S diffractometer (Rigaku, Wrocław, Poland) equipped with a HyPix600HE area-detector (kappa geometry, shutterless ω-scan technique), using graphite monochromatized Cu K_α-radiation; the intensity data were integrated and corrected for absorption and decay

by the CrysAlisPro program [57]. The structures were solved by direct methods using SHELXT [58] and refined on F^2 using SHELXL-2018 [59] or OLEX2 [60].

Electrospray ionization mass spectrometry (ESI–MS). ESI–MS measurements were performed using Maxis and MicroTOF II time-of-flight high-resolution mass spectrometers (Bruker Daltonic GmbH, Bremen, Germany) in positive mode in the mass range of m/z 50–3000. Direct syringe injection was used for all analyzed samples in MeCN solution at a flow rate of 5 μL/min. The capillary voltage was −4500 V, spray shield offset was −500 V, nitrogen nebulizer gas was −1 bar, nitrogen drying gas was 4 L·min^{-1}, and desolvation temperature was 200 °C. The instruments were calibrated with a low concentration tuning mixture (Agilent Technologies G2431A, Santa Clara, CA, USA). Data processing was performed by DataAnalysis 4.0 SP4 software (Bruker Daltonik GmbH, Bremen, Germany).

Melting point measurement. The melting points were measured on a Digital Melting Point Apparatus 1101D (Electrothermal, Stafford, UK).

Transmission electron microscopy (TEM). TEM images of the PdNPs were obtained using a transmission electron microscope HT7700 (Hitachi, Tokyo, Japan) at an accelerating voltage of 100 kV in high resolution mode at a magnification of 80–150 K.

Gas chromatography–mass spectrometry (GC–MS). GC–MS experiments were carried out with a 7890A GC system (Agilent, Santa Clara, CA, USA) equipped with a 5975C mass-selective detector (Agilent, Santa Clara, CA, USA) (electron impact, 70 eV) and an HP-5MS column (30 m × 0.25 mm × 0.25 mm) using He as the carrier gas at a flow of 1.0 mL·min^{-1}.

Dynamic light scattering (DLS). Nanoparticle size measurements were carried out on a ZetaSizer Nano (Malvern, Worcestershire, UK). The temperature of the cell was 25 °C. The data were analyzed with original ZetaSizer software. The radius (R_H) was calculated according to the Stokes–Einstein relation: $D_S = k_B T/6\pi\eta R_H$, in which D_S is the diffusion coefficient, k_B is the Boltzmann constant, T is the absolute temperature, and η is the viscosity. All measurements were performed using 633 nm wavelength at the scattering angle of 173° five times. Only multiple reproducible results were taken into account; therefore, they differed by less than 3%.

2.2. Materials

All procedures associated with the preparation of the starting reagents, synthesis, and isolation of products were carried out under inert atmosphere using the standard Schlenk technique.

Tri-*tert*-butylphosphine (Dal-Chem, Nizhny Novgorod, Russia), methyl and propyl iodides and *n*-alkyl bromides (Sigma-Aldrich, Burlington, MA, USA), phenylboronic acid (Alfa Aesar, Heysham, UK), 1,3,5-tribromobenzene (Alfa Aesar, Heysham, UK), $Pd(OAc)_2$ (Alfa Aesar, Heysham, UK), KOH (Himreaktiv, Stary Oskol, Russia), $NaBF_4$ (Himreaktiv, Stary Oskol, Russia) analytical grade, without additional purification were used in the work. Detailed synthesis and characterization of the phosphonium salts are described in Supplementary Materials.

2.2.1. Typical Procedure for PdNP Preparation

First, 0.0004 g (0.00178 mmol) of palladium acetate and 0.178 mmol of PIL (Supplementary Materials, Table S10) were dissolved in 9 mL ethanol and stirred for 20 min at room temperature. The color of the solution changed from transparent colorless to light brownish gray.

2.2.2. General Procedure for Suzuki Cross-Coupling

To a fresh solution of colloidal Pd, 0.16 g (0.5 mmol) of 1,3,5-tribrombenzene, 0.28 g (2.2 mmol) of phenylboronic acid, and 0.13 g (2.2 mmol) of potassium hydroxide were added. The reaction mixture was stirred over 7 h at 30 °C. Organic compounds were extracted with 9 mL toluene and analyzed by GC–MS.

3. Results and Discussion

3.1. Synthetic Procedures

The quaternization reaction of tri-*tert*-butylphosphine and respective linear 1-haloalkane (Hal = I or Br) was conducted under solvent-free conditions except for the cases with solid haloalkanes. Acetonitrile (for $C_{15}H_{31}Br$) and DMF (for $C_{17}H_{35}Br$) were applied as a solvent (Scheme 1). The temperature of the reaction was varied depending on the applied haloalkane, from −70 °C for MeI [61] to 90–100 °C for liquid 1-bromoalkanes and 80 °C for the solid ones. The reaction was completed after disappearance of the phosphine signal in the ^{31}P NMR spectrum.

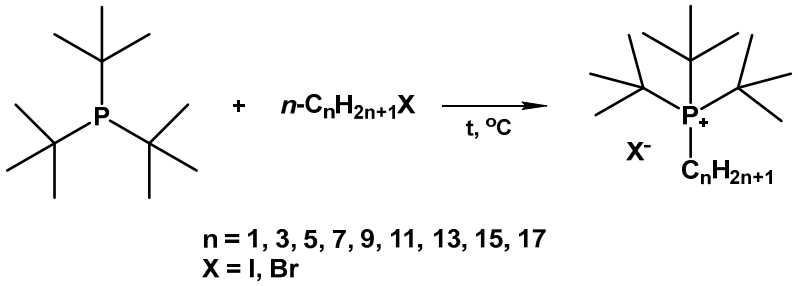

Scheme 1. The quaternization reaction of tri-*tert*-butylphosphine and 1-haloalkane.

The metathesis reaction of phosphonium halide to weakly coordinating tetrafluoroborate-anion was carried out in water at room temperature (Scheme 2). Being poorly soluble in water, phosphonium tetrafluoroborates precipitated as soon as sodium tetrafluoroborate was added to the solution of phosphonium halide, which is readily soluble in water.

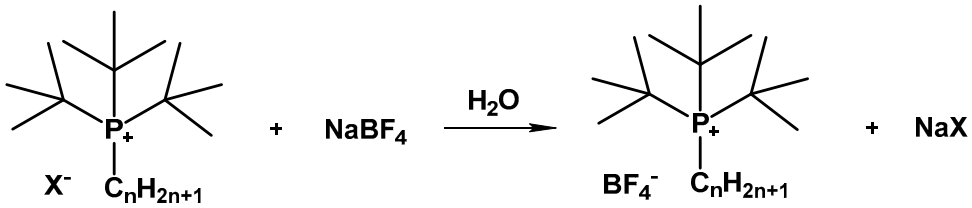

Scheme 2. The anion exchange reaction.

New compounds were obtained in high yields (up to 98%; see Supplementary Materials for details). The phosphonium salts are white or yellowish crystalline or amorphous solids that are soluble in chloroform, dichloromethane, acetone, ethanol, methanol, DMF, DMSO and almost insoluble in diethyl ether and petroleum ether.

3.2. NMR Spectroscopy

3.2.1. ^{31}P NMR Spectral Data

The $^{31}P\{^1H\}$ NMR spectra of the tri-*tert*-butyl(*n*-alkyl)phosphonium salts (Table 1) exhibited a singlet in the range of 47.7–51.3 ppm. The chemical shifts of phosphonium salts weakly depend on the anion. Phosphonium halides have chemical shifts mostly in lower magnetic fields than phosphonium tetrafluoroborates, on average 1–2 ppm. At the same time, the length of the alkyl substituent in the phosphonium cation also has a weak influence on the chemical shift in $^{31}P\{^1H\}$ NMR spectra. The difference is not more than 3.6 ppm. The chemical shifts of **1a** and **1b** appear in a lower magnetic field, possibly due to the lack of electron density of the methyl substituent to compensate for the cationic charge on the phosphorus atom.

3.2.2. ^{1}H NMR Spectral Data

Unlike ^{31}P{^{1}H} NMR spectra, anion exchange has a great influence on the chemical shifts in ^{1}H NMR spectra (Table 1), especially for the α-protons. The α-protons appeared in the ^{1}H NMR spectra as a multiplet (Figure 1).

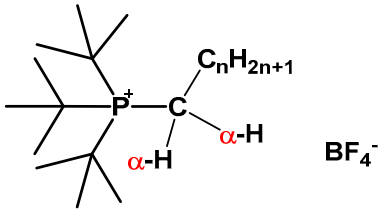

Figure 1. α-Protons in sterically hindered PILs.

Table 1. ^{1}H NMR chemical shifts (δ (ppm), $CDCl_3$, 300.13 MHz, 21 °C) and ^{31}P{^{1}H} NMR chemical shifts (δ (ppm), $CDCl_3$, 121.54 MHz, 21 °C).

Phosphonium Salt			Chemical Shift of α-Protons ^{1}H NMR, ppm	Chemical Shift ^{31}P NMR, ppm
N	**Cation**	**Anion**		
1a	t-$Bu_3P^+CH_3$	I^-	2.11	51.3
1b		BF_4^-	1.90	51.0
2a	t-$Bu_3P^+C_3H_7$	I^-	2.60	50.7
2b		BF_4^-	2.33	49.2
3a	t-$Bu_3P^+C_5H_{11}$	Br^-	2.54	48.8
3b		BF_4^-	2.32	49.2
4a	t-$Bu_3P^+C_7H_{15}$	Br^-	2.56	49.4
4b		BF_4^-	2.29	47.7
5a	t-$Bu_3P^+C_9H_{19}$	Br^-	2.49	49.3
5b		BF_4^-	2.27	47.7
6a	t-$Bu_3P^+C_{11}H_{23}$	Br^-	2.49	50.6
6b		BF_4^-	2.28	48.9
7a	t-$Bu_3P^+C_{13}H_{27}$	Br^-	2.46	50.7
7b		BF_4^-	2.26	48.9
8a	t-$Bu_3P^+C_{15}H_{31}$	Br^-	2.50	50.6
8b		BF_4^-	2.27	48.8
9a	t-$Bu_3P^+C_{17}H_{35}$	Br^-	2.48	50.6
9b		BF_4^-	2.26	48.8

The signal of α-protons in phosphonium tetrafluoroborates appears in a higher magnetic field (2.30 ± 0.03 ppm) than that in phosphonium bromides (2.53 ± 0.07 ppm). This is related to the presence of hydrogen bonds between α-protons and halogen anions bearing high electron affinity. The weakly coordinated tetrafluoroborate anion interacts with the surrounding cations via noncooperative Coulomb forces [62].

The chemical shift of α-protons in ^{1}H NMR spectra moves towards a higher magnetic field with the elongation of the alkyl substituent (Figure 2) due to the compensation of electronic density withdrawn by the cationic charge on the phosphorus atom. The exception is the α-protons of **1a** and **1b,** where the peaks were at 2.11 ppm and 1.90 ppm, respectively, due to belonging to the α-protons of the methyl group.

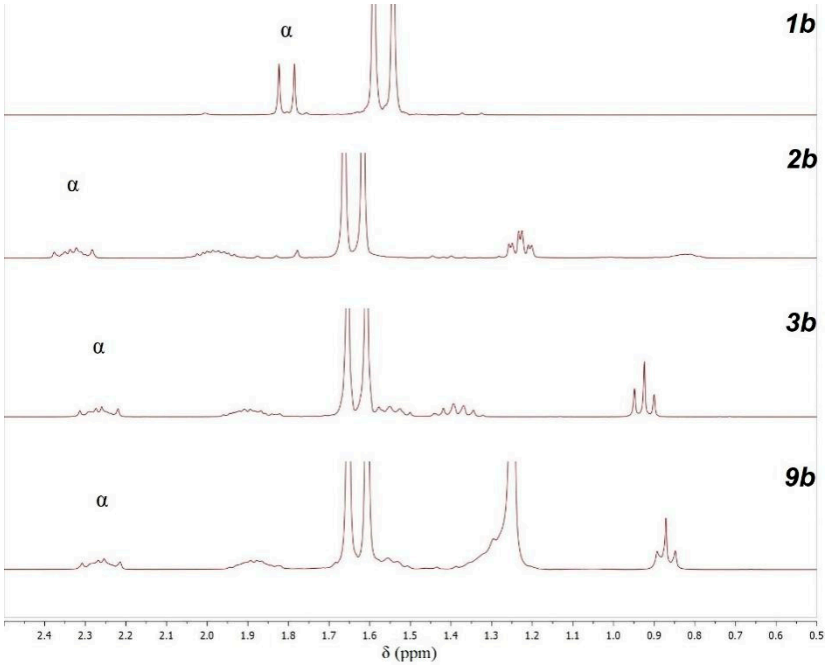

Figure 2. High field area of the ^{1}H NMR spectra ($CDCl_3$, 300.13 MHz, 21 °C) of **1b**, **2b**, **3b** and **9b**.

As the number of methylene groups increases, the shift of the methyl group at the end of the fourth alkyl substituent moves towards a higher magnetic field until it reaches 0.88 ppm (Figure 2). The methylene protons belonging to carbon atoms starting from the fourth one from the phosphorus atom have multiple peaks in the region 1.35–1.20 ppm.

3.2.3. ^{13}C{^{1}H} NMR Spectral Data

A particular pattern in ^{13}C NMR spectra for the investigated PILs is observed. For convenient discussion, we propose labeling the carbon atoms according to Figure 3. The spectra of **1b**, **2b** and **3b** are distinct; for the rest of the PILs, the peak positions are close to each other.

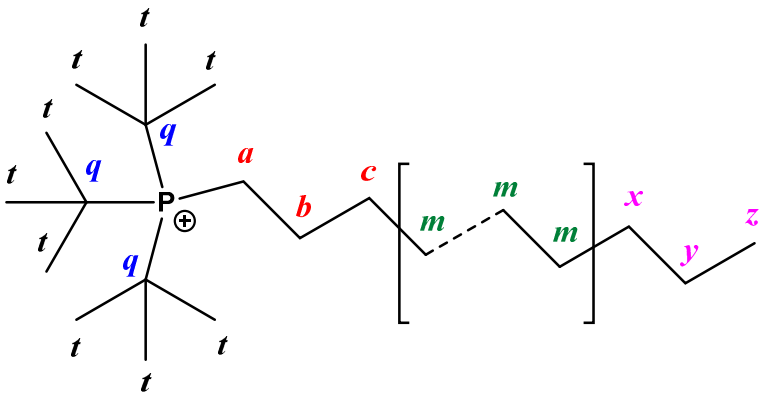

Figure 3. Atom numbering used for the phosphonium cation in discussion of the ^{13}C NMR spectra.

The chemical shift of quaternary carbon atom C_q appears as a doublet at 39.3 ppm with a first-order P-C spin–spin coupling constant of 29.4 ± 0.3 Hz (Figure 3, Table 2). There is one exception for **1b**, whose peak appears at 37.9 ppm, and the first-order P-C coupling constant is 32.1 Hz.

Table 2. $^{13}C\{^{1}H\}$ NMR chemical shifts (δ (ppm), $CDCl_3$, 75.47 MHz, 21 °C), with coupling constants J_{PC} (Hz).

PIL	C_q	C_t	C_a	C_b	C_c	C_m	C_x	C_y	C_z
1b	37.9 (d, $^{1}J_{PC}$ = 32.1)	29.1	0.4 (d, $^{1}J_{PC}$ = 45.8)	-	-	-	-	-	-
2b	39.2 (d, $^{1}J_{PC}$ = 29.4)	29.8	20.4 (d, $^{1}J_{PC}$ = 35.2)	18.9 (d, $^{2}J_{PC}$ = 6.4)	16.3 (d, $^{3}J_{PC}$ = 14.2)	-	-	-	-
3b	39.3 (d, $^{1}J_{PC}$ = 29.1)	29.8	18.5 (d, $^{1}J_{PC}$ = 35.3)	24.7 (d, $^{2}J_{PC}$ = 6.7)	33.7 (d, $^{3}J_{PC}$ = 12.6)	-	-	22.2	13.8
4b	39.3 (d, $^{1}J_{PC}$ = 29.2)	29.8	18.5 (d, $^{1}J_{PC}$ = 35.2)	25.1 (d, $^{2}J_{PC}$ = 6.6)	31.7 (d, $^{3}J_{PC}$ = 12.7)	28.8	31.5	22.6	14.0
5b	39.3 (d, $^{1}J_{PC}$ = 29.3)	29.8	18.5 (d, $^{1}J_{PC}$ = 35.2)	25.0 (d, $^{2}J_{PC}$ = 6.6)	31.7 (d, $^{3}J_{PC}$ = 12.4)	29.3; 29.2	31.8	22.6	14.1
6b	39.3 (d, $^{1}J_{PC}$ = 29.1)	29.8	18.5 (d, $^{1}J_{PC}$ = 34.9)	25.1 (d, $^{2}J_{PC}$ = 6.6)	31.7 (d, $^{3}J_{PC}$ = 12.6)	29.6; 29.4; 29.3; 29.2	31.9	22.7	14.1
7b	39.3 (d, $^{1}J_{PC}$ = 29.4)	29.8	18.5 (d, $^{1}J_{PC}$ = 35.0)	25.0 (d, $^{2}J_{PC}$ = 6.7)	31.7 (d, $^{3}J_{PC}$ = 12.6)	29.6; 29.3; 29.2	31.9	22.7	14.1
8b	39.3 (d, $^{1}J_{PC}$ = 29.4)	29.8	18.5 (d, $^{1}J_{PC}$ = 35.2)	25.0 (d, $^{2}J_{PC}$ = 6.7)	31.7 (d, $^{3}J_{PC}$ = 12.6)	29.7–29.5; 29.4; 29.2	31.9	22.7	14.1
9b	39.3 (d, $^{1}J_{PC}$ = 29.6)	29.8	18.5 (d, $^{1}J_{PC}$ = 35.1)	25.0 (d, $^{2}J_{PC}$ = 6.5)	31.7 (d, $^{3}J_{PC}$ = 12.5)	29.7–29.5; 29.4–29.3; 29.2	31.9	22.7	14.1

The carbon atom of methyl groups in *tert*-butyl C_t does not have the P-C spin–spin coupling constant despite it being located two bonds from the phosphorus atom (Figure 4). This effect could be related to the quaternary carbon atom in between them [62].

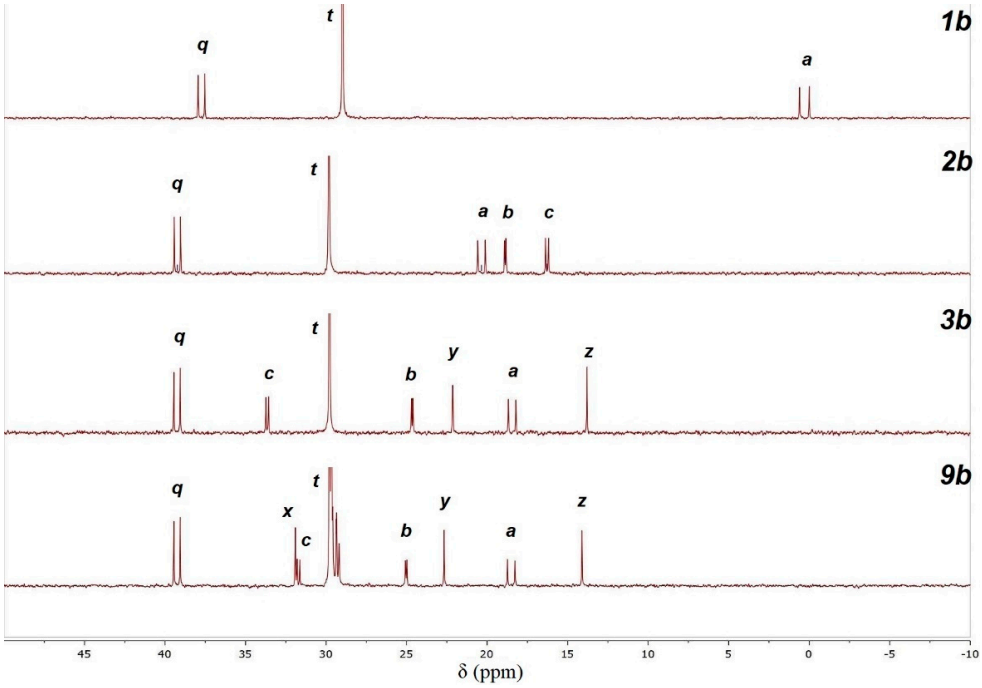

Figure 4. Selected region of the ^{13}C NMR spectra ($CDCl_3$, 75.47 MHz, 21 °C) of **1b**, **2b**, **3b** and **9b**; peaks are assigned according Figure 3.

Three carbon atoms in methylene groups close to the phosphorus atom (C_a, C_b, C_c) appear as doublets with the following P-C spin–spin coupling constant values: 35.1 ± 0.2 Hz, 12.6 ± 0.1 Hz, 6.6 ± 0.1 Hz (Figure 4). On the assumption of 1-D and 2-D NMR spectroscopy (COSY, HSQC, HMBC), we specified the signals of these carbon atoms. We attribute the chemical shift in the ^{13}C NMR spectra with the highest value of the coupling constant to the carbon atom C_a. The peculiar feature of the ^{13}C NMR spectra of **1b** is the position of the C_a peak in the high field (0.4 ppm, Table 2) due to its high shielding. The chemical shift of C_a of **2b** is located at 20.4 ppm. Along with elongation of the alkyl chain, it moves towards a higher field (18.5 ppm). In contrast, the signals of C_b and C_c shift to the lower field (from 18.9 to 25.1 ppm for C_b and from 16.3 to 31.7 ppm for C_c). It should be pointed out that the P-C spin–spin coupling constant for C_b is less than that for C_c (6.4–6.7 Hz and 12.4–14.2 Hz respectively). This could be caused by the steric effect of *tert*-butyl groups (shielding or the possibility of realizing only one certain conformation) or by the influence of the anion.

The chemical shift of the terminal methyl group of the linear alkyl chain C_z is sensitive to the affinity to the phosphorus atom, and it moves towards the lower magnetic field until it reaches 14.1 ppm, which is typical for the methyl group of alkanes.

The signals of the middle carbon atoms (C_m) in the alkyl chain appeared in the range of 28.8–29.7 ppm (Figure 4).

3.3. Single-Crystal X-ray Diffraction Analysis

The structures of **2b**, **3b** and **4b** were determined by the single-crystal X-ray diffraction analysis (Tables S1–S9 and Figures S1–S13 in Supplementary Materials). The asymmetric unit of **2b** contains one $[t\text{-}Bu_3PPr]^+$ cation and one disordered $[BF_4]^-$ anion (Z′ = 1) (Figure 5). It might be noted that only the use of $AgBF_4$ allowed us to obtain pure crystal of **2b**, whereas in the absence of Ag^+, crystals of $[t\text{-}Bu_3PPr]^+[BF_4]^-{}_xI^-{}_{(1-x)}$ (x = 0.94–0.96; e.g., see **2b′**, Figure S2, Tables S4 and S5 in Supplementary Materials) with a substitutional disorder of the anion were formed, in which the iodine atom is located nearly at the boron atom

position. However, the $[BF_4]^-/I^-$ substitutional disorder was not detected for compounds **3b** and **4b** containing a longer *n*-alkyl chain. The asymmetric unit of **3b** (Figure 6) and **4b** (Figure 7) consists of three (Z′ = 3) and of four (Z′ = 4) crystallographically non-equivalent $[t\text{-}Bu_3P(n\text{-}C_nH_{2n+1})]^+[BF_4]^-$ ion pairs, correspondingly. In case of **4b**, six out of eight ions were entirely disordered (Figures S8–S13, Tables S8 and S9 in Supplementary Materials).

Enlargement of the alkyl chain likely leads to increase in a number of crystallographically independent ion pairs (Z′) and disorder augmentation. The crystal packing of sterically hindered PILs with significantly different length of alkyl substituent was reported earlier [54].

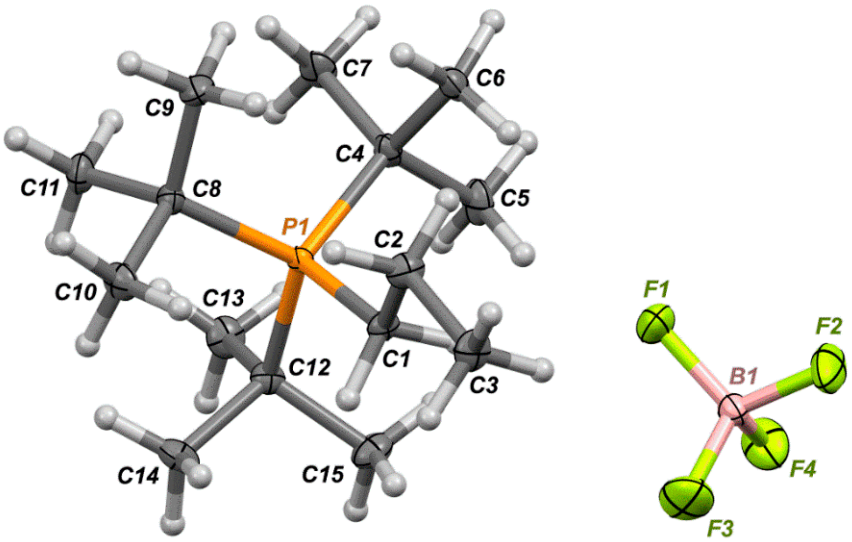

Figure 5. Crystal structure of **2b**. The disorder of the BF_4^- anion is not shown. Hereinafter the probability of thermal ellipsoids is set to the 50% level.

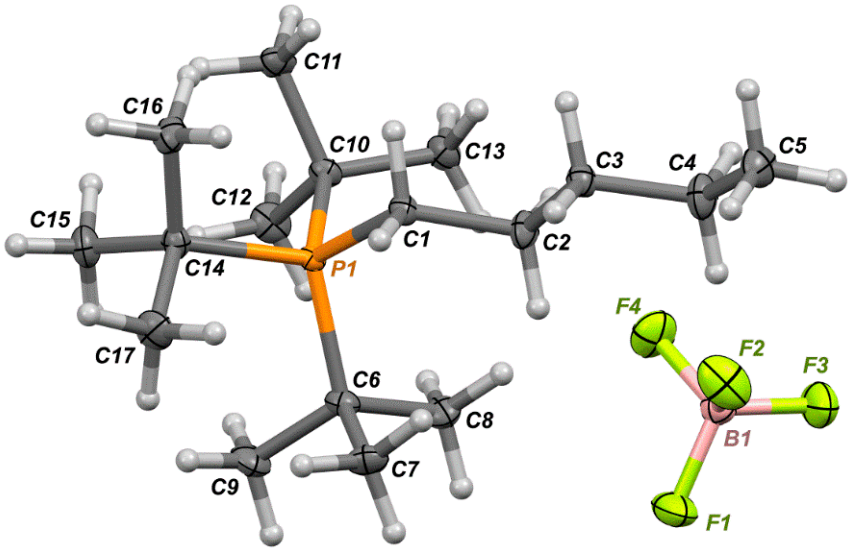

Figure 6. Crystal structure of **3b**. One of three non-equivalent ion pairs is shown.

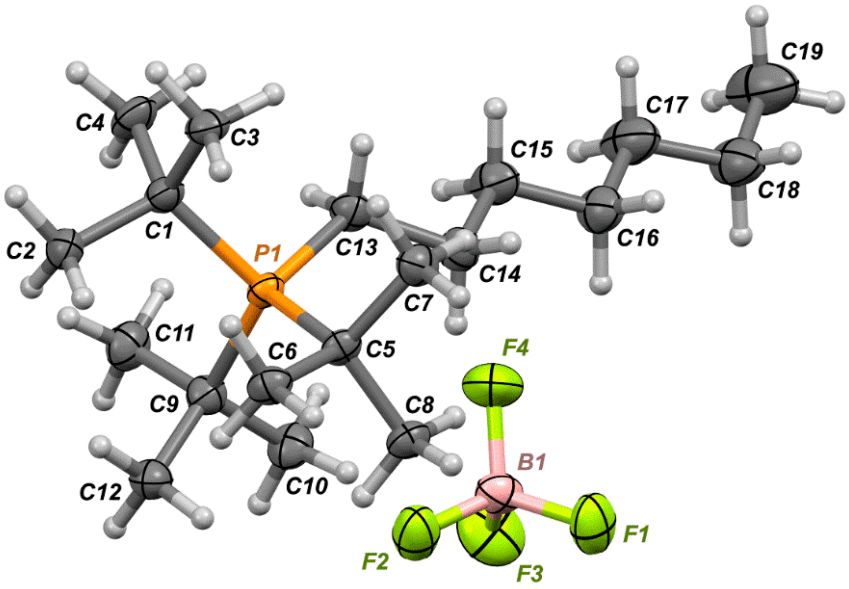

Figure 7. Crystal structure of **4b**. One of four crystallographically non-equivalent ion pairs is shown.

3.4. Melting Point

The melting point (T_m) of the synthesized PILs was measured. The trend of T_m as a function of the number of carbon atoms in the alkyl substituent of PIL is presented in Figure 8.

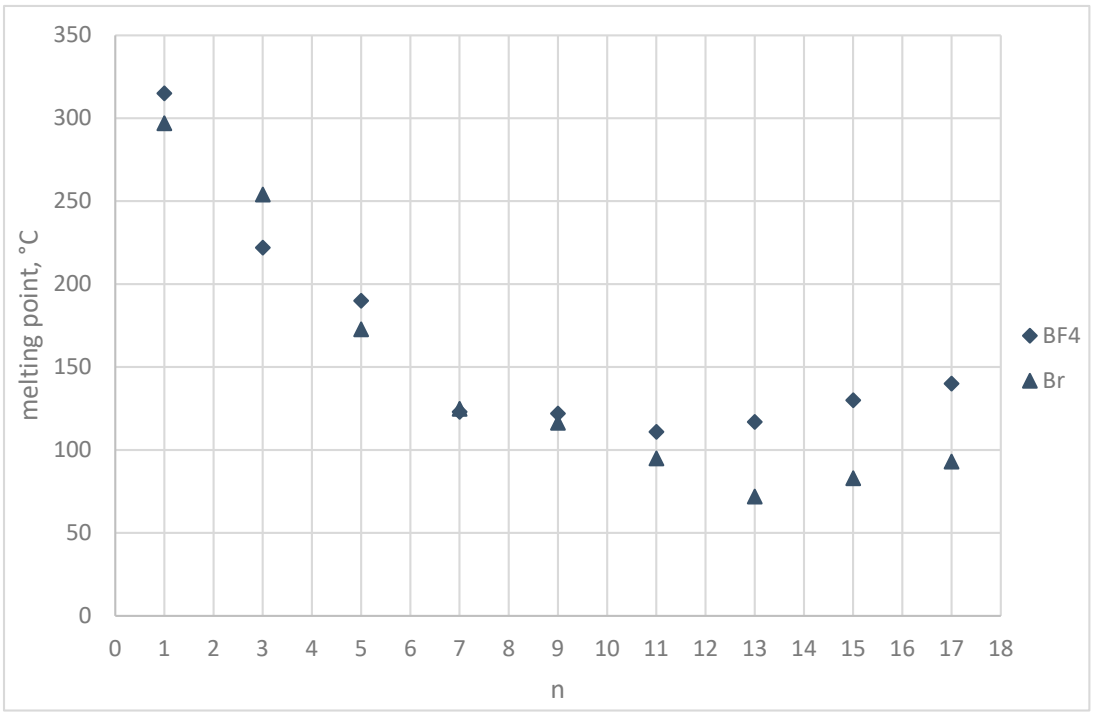

Figure 8. Melting points as a function of the number of carbons, *n*, in the fourth alkyl substituent on the phosphorus atom.

The first two members of the PIL series have high melting points above 200 °C and melt with decomposition that is caused by the pronounced ionic nature of the compounds. The moderate size of the phosphonium cation and its relative symmetry cause high lattice energy. With an increase in the methylene groups in the alkyl chain, T_m diminishes stepwise and reaches a minimum. This fact is connected with the gain of disordering in the crystal

lattice. The next slight increase in the melting point of long-chained PILs is caused by hydrophobic intermolecular interactions. The corresponding dependence of T_m on the elongation of alkyl substituents in the series of homologous compounds was reported earlier [54,63].

The anion has a moderate influence on the melting point of PIL. The difference is minor for medium-length chained ionic liquids and slightly greater for outer members in the row. It should be noted that **4a** and **4b** have almost the same melting point (approximately 125 °C). The T_m values of phosphonium bromides in most cases are lower than those for phosphonium tetrafluoroborates. The fluorine atoms have short contacts with hydrogen atoms belonging to the linear alkyl chain, resulting in an increase in intermolecular interactions. It is remarkable that **6a**, **7a**, **8a** and **9a** melt below 100 °C.

3.5. PdNP Stabilization and TEM Sample Preparation

PILs have been proven to be an effective stabilizer of metal nanoparticles [5,64]. The application of stabilized NPs is widespread in the area of catalysis [65] and other areas. ILs could be also involved in the creation of novel nanocomposites with biopolymers for drug and gene delivery [66]. In addition, ILs could be applied for magnetic NP stabilization to extract heavy metal ions [67].

For the current study, PdNPs were obtained by the reduction of palladium acetate in ethanol in the presence of the corresponding PIL (Supplementary Materials, Table S10). According to previous investigation, ethanol is the solvent of choice for efficient synthesis of hybrid NP systems [54]. The PdNP synthesis procedure does not require any reducing agent, elevated temperature or inert atmosphere. The PdNP size was estimated using transmission electron microscopy (TEM) (Figure 9). The "nanofishing" technique was used to capture nanoparticles from the liquid phase. The copper grid was immersed in a colloidal solution of the PdNPs for 30 s, rinsed with acetone to remove organic components and dried in air.

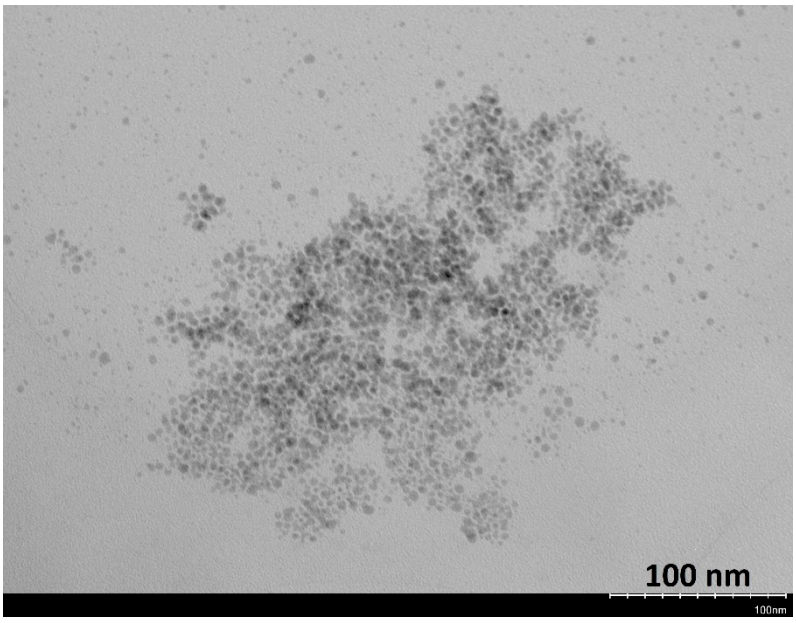

Figure 9. TEM image of PdNPs stabilized with **9b**.

Here, the key point of the present study should be emphasized. A common procedure involves drying the solution and then using the obtained solid phase for microscopic analysis. However, in such a case, nanoparticles may form during the drying process, or their morphology may substantially change upon drying. In the present study, we captured nanoparticles directly from solution without carrying out a destructive isolation/drying process.

3.6. PdNP Behavior during Suzuki Reaction

Freshly prepared PdNPs were involved in the Suzuki cross-coupling reaction (Scheme 3) as a catalyst. Pd (0.36 mol%) and the molar ratio of stabilizer/Pd 100/1 were used as optimal (Table S10). The GC–MS method was used to estimate the conversion degree of 1,3,5-tribromobenzene into 1,3,5-triphenylbenzene. It should be noted that triphenylbenzene was formed as a main product.

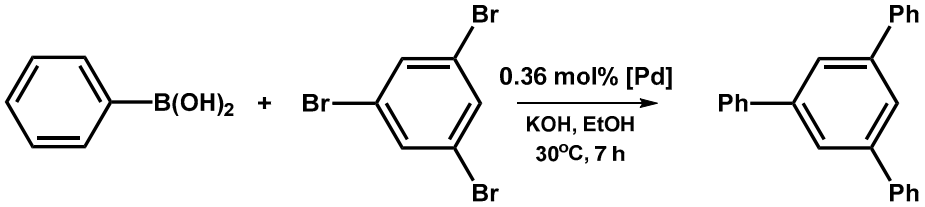

Scheme 3. Suzuki cross-coupling reaction of 1,3,5-tribromobenzene and phenylboronic acid.

The challenging tri-substituted substrate and mild conditions of the catalytic reaction were chosen to emphasize the difference between the catalytic systems based on PILs of different structures. The conversion of 1,3,5-tribromobenzene into 1,3,5-triphenylbenzene is a good benchmarking system, which we used here to analyze the behavior of the particular studied catalytic system in the cross-coupling reaction.

The preparation of the PdNPs for TEM analysis was carried out after 20 min of stirring the phosphonium salt and palladium acetate in ethanol and 7 h after the start of the cross-coupling reaction using the "nanofishing" technique. For each entry, 100–500 nanoparticles were processed to calculate the average size and standard deviation (Table 3, Figures S14–S31 in Supplementary Materials). There were aggregates and individual PdNPs in the TEM images. Most of them were uniform and had clear edges.

Table 3. The average size of PdNPs before and after the Suzuki reaction.

Entry	PIL	The Average Size of PdNPs, nm	The Average Size of PdNPs after Suzuki Reaction, nm
1	**1b**	7.3 ± 1.5	3.0 ± 1.2
2	**2b**	5.1 ± 3.0	5.0 ± 1.6
3	**3b**	3.7 ± 0.9	4.6 ± 1.3
4	**4b**	2.8 ± 0.9	2.8 ± 1.0
5	**5b**	4.5 ± 3.1	5.8 ± 3.0
6	**6b**	3.2 ± 0.8	2.9 ± 1.0
7	**7b**	4.1 ± 1.2	3.7 ± 1.1
8	**8b**	4.2 ± 1.2	3.5 ± 1.0
9	**9b**	3.6 ± 1.4	2.6 ± 0.9

These systems were studied in terms of nanoparticle stabilization by coating agents of various natures. There are three types of NP stabilization: electrostatic, steric and electrosteric (a transitional one) [68,69]. The electrostatic type of NP stabilization is typical for ionic compounds. The hydrophobic long alkyl chain in the structure provides steric stabilization. Extreme electrostatic and steric types lead to the strong stabilization of NPs and affect their surface inacceptability [70,71]. The combined type of stabilization is electrosteric when the compound has an ionic charge as well as hydrophobic alkyl chain. Mostly the ILs provide electrosteric stabilization. The series of bulky phosphonium salts under investigation has structural diversity, and all types of stabilization are represented in a row.

PILs with short alkyl chains and hydrophilic properties usually provide electrostatic stabilization. The compounds **1b** and **2b** have a stronger ionic nature in the range and, as a consequence, could not effectively prevent PdNP agglomeration. The NP size in **1b** after the reaction decreased more than twice (Table 3, entry 1), which could be explained

by aggregation of the large PdNPs, their precipitation and excluding from the system. At the same time, an amount of small NPs of approximately 3 nm remained in the reaction mixture. Despite the same mean PdNP size of **2b**, the size distribution decreased during the catalytic reaction, which has a similar explanation as occurred with **1b**.

Chain elongation results in a higher contribution of steric stabilization and, as a consequence, a decrease in the mean PdNP size and size distribution.

Compound **5b** has a middle alkyl substituent length and steric reasons begin to prevail in PdNP stabilization. Due to its molecular nature, **5b** could stabilize larger PdNPs as well as smaller ones, and the size distribution significantly increased. In Figures S22 and S23 (in Supplementary Materials), we observe a bimodal system of the particles: the first group has mean sizes of 3–5 nm, and the second has sizes of 11–13 nm, respectively.

PILs **6b–9b,** due to steric reasons, could stabilize PdNPs in the initial stage of nucleation, providing the presence of a large number of small particles (2.6–4.2 nm) with a narrow size distribution.

The change in PdNP size depending on the length of the fourth substituent observed in the present article is similar to the trends described previously for PILs with even numbers of carbon atoms in the side alkyl chain [54].

The implication of the bulky PIL for PdNP stabilization allows good and moderate conversion of 34–62% (Figure 10). Catalytic systems including PILs with medium-sized alkyl substituents possess slightly higher activity than other PILs. The dynamic nature of the nanocatalyst requires a balance between its activity and stability that could be provided by a stabilizer combining electrostatic and steric properties.

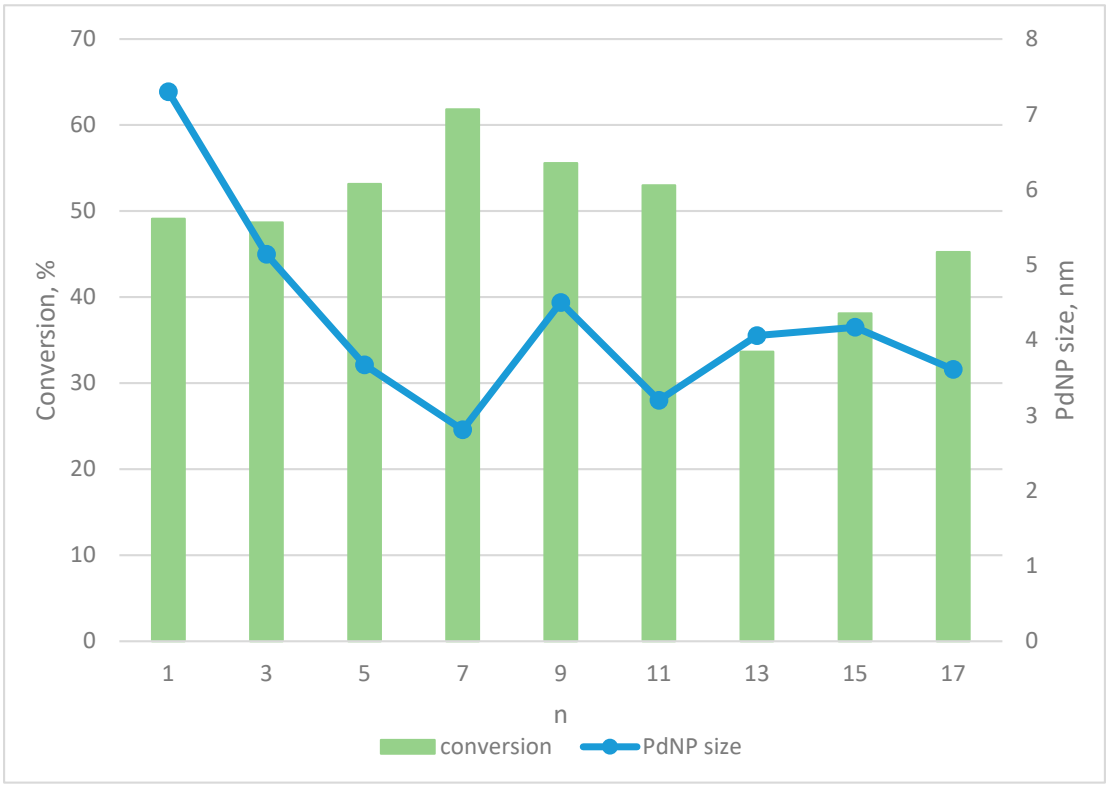

Figure 10. The PdNP size and the conversion of the Suzuki reaction depend on the phosphonium salt structure.

3.7. DLS Data of the Catalytic System

The catalytic composition includes palladium, PIL and solvent molecules. TEM images show assembled clusters of PdNPs that could contain PILs as well. One may suggest the presence of such metal-organic aggregates in solution before and during the catalytic

reaction. We used an affordable DLS technique to determine the size of the nanocomposite in solution.

Catalytic systems including **4b**–**9b** were studied, and bimodality was found to be a characteristic feature. Two groups of particles of various sizes were observed. The hydrodynamic diameter of metal-organic aggregates changes regularly in the PIL row. The catalytic composition consisting of **4b**, **5b**, **8b** and **9b** was characterized by a large amount (94–98%) of smaller particles measuring 238–371 nm (Table 4, Figures S32–S37 in Supplementary Materials). The proportion between small and large aggregates changes for **6b**. This system contains 68% small particles (219 nm), and 32% of the remaining particles have a mean size of 678 nm. In the case of **7b,** the distribution in the system became completely monomodal (large aggregates with an average size of 840 nm).

Table 4. The size of nanocomposites in ethanol solution.

Entry	PIL	Size of Nanocomposites (nm)
1	**4b**	309 ± 2
2	**5b**	371 ± 2
3	**6b**	219 ± 3
4	**7b**	842 ± 5
5	**8b**	304 ± 2
6	**9b**	238 ± 2

Notably, the catalyst based on **7b** demonstrates the lowest conversion in the row. At the same time, it is the only monomodal system with larger particles. Consequently, metal-organic aggregates of approximately 800 nm weakly promote the Suzuki reaction compared to the above smaller particles. The prevalence of small particles in the solution contributes to the catalytic activity of PdNPs (**6b** and **9b**). However, the system with **8b** includes small particles and shows only slightly increased conversion compared to the **7b** system. Thus, the correlation between the aggregate size and the conversion is not clear. Most likely, the inner structure of observable metal-organic aggregates is essential.

Concerning the study of the catalytic system, one may note the following discussion. The sizes of the PdNPs varied in the range of 2.6–7.3 nm, which can affect the catalytic activity through the quantity of the surface active atoms of Pd [72], but this was not the case. A similar scenario appears when DLS measurement of the catalytic system was performed. The complexity and multifactorial nature of the catalytic process indicate that different palladium particles could be reservoirs for active species [73]. The stage of oxidative addition of the reagent to Pd or the leaching process results in small active clusters or even atomic Pd [74,75]. The high catalytic activity of such dissimilar catalysts indicates the presence of a dynamic catalytic system [74]. In this situation, the initial size of the PdNPs does not significantly influence the catalytic activity.

In case of the metal-organic particles, their inner structure is more essential rather than their size. The nearest environment of the Pd(0) consisting of the PIL ions influences the catalytic activity. It is caused by migration of the reactant to the surface of PdNP, reverse movement of the reaction products, Pd clusters and atoms leaching. The supramolecular network of the metal-organic aggregate derives from the structure directionality of the particular PIL that is known in the literature as microheterogeneity [37,76] and possessed by all types of ILs. For this reason an extensive study of the PIL microstructure is required.

4. Conclusions

A family of new phosphonium ionic liquids containing bulky cations based on tri-*tert*-butylphosphine with varied *n*-alkyl substituents was synthesized and characterized. A detailed study of their ^{1}H, ^{13}C and ^{31}P NMR spectra, melting points, mass spectra and single-crystal X-ray diffraction analysis was performed. The diversity of represented PIL members allows us to demonstrate a nonlinear relationship between structure and properties. Despite their similar structure, notable differences occurred in NMR spectra,

melting points, size and distribution of stabilized PdNPs as well as in their catalytic performance. PILs were declared tunable compounds with desired properties and an effective PdNP stabilizer, which are advantages for their usage in industrial and academic practice. PILs are capable of forming and stabilizing aggregates with Pd(0), which are clearly identified by TEM and DLS analyses. The size and catalytic activity of metal-organic aggregates depend on the PIL structure at the molecular level and on the nature of the intermolecular interaction.

The appropriate prospect for the study of sterically hindered PILs is their microstructure investigation. Obviously, the possible practical use of PILs requires new insight into their impact on the environment. Therefore, their toxicity against microorganisms and human cells should be estimated.

Supplementary Materials: The following are available online at https://www.mdpi.com/article/10.3390/su13179862/s1, Materials, Synthetic procedures, $^{1}H/^{13}C/^{31}P$ NMR spectra for all compounds. Crystal data, data collection and structure refinement details for **2b**, **2b′**, **3b** and **4b** are summarized in Table S1. The structures have been deposited at the Cambridge Crystallographic Data Center with the reference CCDC numbers 2099141-2099145; they also contain supplementary crystallographic data. These data can be obtained free of charge from the CCDC via https://www.ccdc.cam.ac.uk/structures/ (accessed on 01 september 2021). Table S1. Crystal data and structure refinement for **2b**. Table S2. Bond lengths for **2b**/Å. Table S3. Bond angles for **2b**/°. Table S4. Bond lengths for **2b′**/Å. Table S5. Bond angles for **2b′**/°. Table S6. Bond lengths for **3b**/Å. Table S7. Bond angles for **3b**/°. Table S8. Bond lengths for **4b**/Å. Table S9. Bond angles for **4b**/°. Table S10. The mass of PIL used in the procedure of catalyst preparation. Figure S1. The structure of **2b**. The $[BF_4]^-$ anion is disordered over two positions (*A* and *B*) with the disorder ratio of 0.855(9):0.145(9). The displacement ellipsoids are set to the 50% probability level. Figure S2. The structure of **2b′**. The disorder ratio for the $[BF_4]^-/I^-$ positional disorder is 0.9614(4):0.0386(4). The displacement ellipsoids are set to the 50% probability level. Figure S3. Crystallographically non-equivalent ions of **3b**. The displacement ellipsoids are set to the 50% probability level. Figure S4. The first crystallographically non-equivalent cation $[^{t}Bu_3P(n\text{-}C_5H_{11})]^+$ in **3b**. The displacement ellipsoids are set to the 50% probability level. Figure S5. The second crystallographically non-equivalent cation $[^{t}Bu_3P(n\text{-}C_5H_{11})]^+$ in **3b**. The displacement ellipsoids are set to the 50% probability level. Figure S6. The third crystallographically non-equivalent cation $[^{t}Bu_3P(n\text{-}C_5H_{11})]^+$ in **3b**. The displacement ellipsoids are set to the 50% probability level. Figure S7. Three crystallographically non-equivalent anions $[BF_4]^-$ in **3b**. The displacement ellipsoids are set to the 50% probability level. Figure S8. Crystallographically non-equivalent cations $[^{t}Bu_3P(n\text{-}C_7H_{15})]^+$ and anions $[BF_4]^-$ in **4b**. The disorder is not shown. Hydrogen atoms are omitted. The displacement ellipsoids are set to the 50% probability level. Figure S9. The first crystallographically non-equivalent cation $[^{t}Bu_3P(n\text{-}C_7H_{15})]^+$ in **4b**. Hydrogen atoms are omitted. The displacement ellipsoids are set to the 50% probability level. Figure S10. The second crystallographically non-equivalent cation $[^{t}Bu_3P(n\text{-}C_7H_{15})]^+$ in **4b**. Hydrogen atoms are omitted. The displacement ellipsoids are set to the 50% probability level. The A/B disorder ratio is 0.904(2): 0.096(2) for three ^{t}Bu fragments and 0.772(4):0.228(4) for the $n\text{-}C_7H_{15}$ aliphatic chain. Figure S11. The third crystallographically non-equivalent cation $[^{t}Bu_3P(n\text{-}C_7H_{15})]^+$ in **4b**. Hydrogen atoms are omitted. The displacement ellipsoids are set to the 50% probability level. The A/B disorder ratio is 0.6176(16):0.3824(16). Figure S12. The fourth crystallographically non-equivalent cation $[^{t}Bu_3P(n\text{-}C_7H_{15})]^+$ in **4b**. Hydrogen atoms are omitted. The displacement ellipsoids are set to the 50% probability level. The A/B disorder ratio is 0.8810(16):0.1190(16). Figure S13. Four crystallographically non-equivalent anion $[BF_4]^-$ in **4b**. The displacement ellipsoids are set to the 50% probability level. The A/B disorder ratio for atoms B2, F5..F8 is 0.884(8):0.116(8). The A/B/C disorder ratio for atoms F10..F12 is 0.515(3):0.198(3):0.087(2). The A/B/C disorder ratio for atoms B4, F13..F16 is 0.753(3):0.133(3):0.114(2). Figure S14. TEM image (a) and size distribution (b) of PdNPs in **1b** before the Suzuki reaction. Figure S15. TEM image (a) and size distribution (b) of PdNPs in **1b** after the Suzuki reaction. Figure S16. TEM image (a) and size distribution (b) of PdNPs in **2b** before the Suzuki reaction. Figure S17. TEM image (a) and size distribution (b) of PdNPs in **2b** after the Suzuki reaction. Figure S18. TEM image (a) and size distribution (b) of PdNPs in **3b** before the Suzuki reaction. Figure S19. TEM image (a) and size distribution (b) of PdNPs in **3b** after the Suzuki reaction. Figure S20. TEM image (a) and size distribution (b) of PdNPs

in **4b** before the Suzuki reaction. Figure S21. TEM image (a) and size distribution (b) of PdNPs in **4b** after the Suzuki reaction. Figure S22. TEM image (a) and size distribution (b) of PdNPs in **5b** before the Suzuki reaction. Figure S23. TEM image (a) and size distribution (b) of PdNPs in **5b** after the Suzuki reaction. Figure S24. TEM image (a) and size distribution (b) of PdNPs in **6b** before the Suzuki reaction. Figure S25. TEM image (a) and size distribution (b) of PdNPs in **6b** after the Suzuki reaction. Figure S26. TEM image (a) and size distribution (b) of PdNPs in **7b** before the Suzuki reaction. Figure S27. TEM image (a) and size distribution (b) of PdNPs in **7b** after the Suzuki reaction. Figure S28. TEM image (a) and size distribution (b) of PdNPs in **8b** before the Suzuki reaction. Figure S29. TEM image (a) and size distribution (b) of PdNPs in **8b** after the Suzuki reaction. Figure S30. TEM image (a) and size distribution (b) of PdNPs in **9b** before the Suzuki reaction. Figure S31. TEM image (a) and size distribution (b) of PdNPs in **9b** after the Suzuki reaction. Figure S32. The size distribution of metal-organic aggregates in solution of catalytic system based on **4b.** Figure S33. The size distribution of metal-organic aggregates in solution of catalytic system based on **5b.** Figure S34. The size distribution of metal-organic aggregates in solution of catalytic system based on **6b.** Figure S35. The size distribution of metal-organic aggregates in solution of catalytic system based on **7b.** Figure S36. The size distribution of metal-organic aggregates in solution of catalytic system based on **8b.** Figure S37. The size distribution of metal-organic aggregates in solution of catalytic system based on **9b.**

Author Contributions: D.M.A., V.V.E., F.G.V., G.A.G., M.E.M. carried out the experimental work and measured and analyzed the data. V.P.A., V.A.M., L.Y.Z. created the idea, designed and planned the study, and supervised the whole project. All authors discussed the results, contributed to writing the manuscript and approved the final version of the manuscript for submission. All authors have read and agreed to the published version of the manuscript.

Funding: This research was funded by RFBR (project number 19-33-60074).

Acknowledgments: The authors gratefully acknowledge the CSF-SAC FRC KSC RAS for providing necessary facilities to carry out this work. Crystal structure determination was performed in the Department of Structural Studies of Zelinsky Institute of Organic Chemistry, Moscow.

Conflicts of Interest: The authors declare no conflict of interest.

References

1. Plechkova, N.V.; Seddon, K.R. Applications of ionic liquids in the chemical industry. *Chem. Soc. Rev.* **2008**, *37*, 123–150. [CrossRef] [PubMed]
2. Huang, Y.; Chen, Z.; Crosthwaite, J.M.; Aki, S.N.; Brennecke, J.F. Thermal Stability of Ionic Liquids in Nitrogen and Air Environments. *J. Chem. Thermodyn.* **2021**, *161*, 106560. [CrossRef]
3. Hallett, J.P.; Welton, T. Room-Temperature Ionic Liquids: Solvents for Synthesis and Catalysis. 2. *Chem. Rev.* **2011**, *111*, 3508–3576. [CrossRef]
4. Łuczak, J.; Paszkiewicz-Gawron, M.; Krukowska, A.; Malankowska, A.; Zaleska-Medynska, A. Ionic liquids for nano- and microstructures preparation. Part 1: Properties and multifunctional role. *Adv. Colloid Interface Sci.* **2016**, *230*, 13–28. [CrossRef]
5. Khazalpour, S.; Yarie, M.; Kianpour, E.; Amani, A.; Asadabadi, S.; Seyf, J.Y.; Rezaeivala, M.; Azizian, S.; Zolfigol, M.A. Applications of phosphonium-based ionic liquids in chemical processes. *J. Iran. Chem. Soc.* **2020**, *17*, 1775–1917. [CrossRef]
6. Egorova, K.; Ananikov, V.P. Fundamental importance of ionic interactions in the liquid phase: A review of recent studies of ionic liquids in biomedical and pharmaceutical applications. *J. Mol. Liq.* **2018**, *272*, 271–300. [CrossRef]
7. Gabriel, S.; Weiner, J. Ueber einige Abkömmlinge des Propylamins. *Eur. J. Inorg. Chem.* **1888**, *21*, 2669–2679. [CrossRef]
8. Walden, P. Molecular weights and electrical conductivity of several fused salts. *Bull. Acad. Imper. Sci. St. Petersburg* **1914**, *1800*, 405–422.
9. Welton, T. Ionic liquids: A brief history. *Biophys. Rev.* **2018**, *10*, 691–706. [CrossRef]
10. Lawal, I.A.; Klink, M.; Ndungu, P.; Moodley, B. Brief bibliometric analysis of "ionic liquid" applications and its review as a substitute for common adsorbent modifier for the adsorption of organic pollutants. *Environ. Res.* **2019**, *175*, 34–51. [CrossRef] [PubMed]
11. Morton, M.D.; Hamer, C.K. Ionic liquids—The beginning of the end or the end of the beginning?—A look at the life of ionic liquids through patent claims. *Sep. Purif. Technol.* **2018**, *196*, 3–9. [CrossRef]
12. Watanabe, M.; Thomas, M.L.; Zhang, S.; Ueno, K.; Yasuda, T.; Dokko, K. Application of Ionic Liquids to Energy Storage and Conversion Materials and Devices. *Chem. Rev.* **2017**, *117*, 7190–7239. [CrossRef]
13. Karuppasamy, K.; Theerthagiri, J.; Vikraman, D.; Yim, C.-J.; Hussain, S.; Sharma, R.; Maiyalagan, T.; Qin, J.; Kim, H.-S. Ionic Liquid-Based Electrolytes for Energy Storage Devices: A Brief Review on Their Limits and Applications. *Polymers* **2020**, *12*, 918. [CrossRef]

14. Osada, I.; De Vries, H.; Scrosati, B.; Passerini, S. Ionic-Liquid-Based Polymer Electrolytes for Battery Applications. *Angew. Chem. Int. Ed.* **2016**, *55*, 500–513. [CrossRef]
15. Lecce, D.D.; Hassoun, J. Lithium Metal Battery Using $LiFe_{0.5}Mn_{0.5}PO_4$ Olivine Cathode and Pyrrolidinium-Based Ionic Liquid Electrolyte. *ACS Omega* **2018**, *3*, 8583–8588. [CrossRef] [PubMed]
16. Vaalma, C.; Buchholz, D.; Weil, M.; Passerini, S. A cost and resource analysis of sodiumion batteries. *Nat. Rev. Mater.* **2018**, *3*, 18013. [CrossRef]
17. Chagas, L.G.; Jeong, S.; Hasa, I.; Passerini, S. Ionic Liquid-Based Electrolytes for Sodium-Ion Batteries: Tuning Properties to Enhance the Electrochemical Performance of Manganese-Based Layered Oxide Cathode. *ACS Appl. Mater. Interfaces* **2019**, *11*, 22278–22289. [CrossRef]
18. Opallo, M.; Lesniewski, A. A review on electrodes modified with ionic liquids. *J. Electroanal. Chem.* **2011**, *656*, 2–16. [CrossRef]
19. Khrizanforov, M.; Shekurov, R.; Miluykov, V.; Gilmanova, L.; Kataeva, O.; Yamaleeva, Z.; Gerasimova, T.; Ermolaev, V.; Gubaidullin, A.; Laskin, A.; et al. Excellent supercapacitor and sensor performance of robust cobalt phosphinate ferrocenyl organic framework materials achieved by intrinsic redox and structure properties. *Dalton Trans.* **2019**, *48*, 16986–16992. [CrossRef]
20. Egorova, K.S.; Gordeev, E.G.; Ananikov, V.P. Biological Activity of Ionic Liquids and Their Application in Pharmaceutics and Medicine. *Chem. Rev.* **2017**, *117*, 7132–7189. [CrossRef]
21. Claus, J.; Sommer, F.O.; Kragl, U. Ionic liquids in biotechnology and beyond. *Solid State Ionics* **2018**, *314*, 119–128. [CrossRef]
22. Xue, Y.; Xiao, H.; Zhang, Y. Antimicrobial Polymeric Materials with Quaternary Ammonium and Phosphonium Salts. *Int. J. Mol. Sci.* **2015**, *16*, 3626–3655. [CrossRef] [PubMed]
23. Ferraz, R.; Costa-Rodrigues, J.; Fernandes, M.H.; Santos, M.; Marrucho, I.; Rebelo, L.P.; Prudêncio, C.; Noronha, J.P.; Željko, P.; Branco, L.C. Antitumor Activity of Ionic Liquids Based on Ampicillin. *ChemMedChem* **2015**, *10*, 1480–1483. [CrossRef] [PubMed]
24. Shamshina, J.L.; Rogers, R.D. Are Myths and Preconceptions Preventing us from Applying Ionic Liquid Forms of Antiviral Medicines to the Current Health Crisis? *Int. J. Mol. Sci.* **2020**, *21*, 6002. [CrossRef]
25. Liu, Z.-W.; Yue, Z.; Zeng, X.-A.; Cheng, J.-H.; Aadil, R.M. Ionic liquid as an effective solvent for cell wall deconstructing through astaxanthin extraction from Haematococcus pluvialis. *Int. J. Food Sci. Technol.* **2018**, *54*, 583–590. [CrossRef]
26. Verma, C.; Mishra, A.; Chauhan, S.; Verma, P.; Srivastava, V.; Quraishi, M.; Ebenso, E.E. Dissolution of cellulose in ionic liquids and their mixed cosolvents: A review. *Sustain. Chem. Pharm.* **2019**, *13*, 100162. [CrossRef]
27. Somers, A.E.; Howlett, P.C.; Macfarlane, D.R.; Forsyth, M. A Review of Ionic Liquid Lubricants. *Lubricants* **2013**, *1*, 3–21. [CrossRef]
28. Ge, X.; Li, J.; Wang, H.; Zhang, C.; Liu, Y.; Luo, J. Macroscale superlubricity under extreme pressure enabled by the combination of graphene-oxide nanosheets with ionic liquid. *Carbon* **2019**, *151*, 76–83. [CrossRef]
29. Avilés, M.; Sánchez, C.; Pamies, R.; Sanes, J.; Bermúdez, M. Ionic Liquid Crystals in Tribology. *Lubricants* **2019**, *7*, 72. [CrossRef]
30. Hejazifar, M.; Lanaridi, O.; Bica-Schröder, K. Ionic liquid based microemulsions: A review. *J. Mol. Liq.* **2020**, *303*, 112264. [CrossRef]
31. Kissoudi, M.; Samanidou, V. Recent Advances in Applications of Ionic Liquids in Miniaturized Microextraction Techniques. *Molecules* **2018**, *23*, 1437. [CrossRef]
32. Wassershied, P.; Keim, W. Ionic Liquids-New "Solutions" for Transition Metal Catalysis. *Angew. Chem. Int. Ed.* **2000**, *39*, 3772–3789. [CrossRef]
33. Pensado, A.S.; Padua, A. Solvation and Stabilization of Metallic Nanoparticles in Ionic Liquids. *Angew. Chem. Int. Ed.* **2011**, *50*, 8683–8687. [CrossRef]
34. Yin, L.; Liebscher, J. Carbon−Carbon Coupling Reactions Catalyzed by Heterogeneous Palladium Catalysts. *Chem. Rev.* **2007**, *107*, 133–173. [CrossRef] [PubMed]
35. Scholten, J.D.; Leal, B.C.; Dupont, J. Transition Metal Nanoparticle Catalysis in Ionic Liquids. *ACS Catal.* **2011**, *2*, 184–200. [CrossRef]
36. Vekariya, R.L. A review of ionic liquids: Applications towards catalytic organic transformations. *J. Mol. Liq.* **2017**, *227*, 44–60. [CrossRef]
37. Wang, Y.-L.; Li, B.; Sarman, S.; Mocci, F.; Lu, Z.-Y.; Yuan, J.; Laaksonen, A.; Fayer, M.D. Microstructural and Dynamical Heterogeneities in Ionic Liquids. *Chem. Rev.* **2020**, *120*, 5798–5877. [CrossRef]
38. Parajó, J.J.; Vallet, P.; Fernádez-Míguez, L.; Villanueva, M.; Salgado, J. Ecotoxicity of Mixtures of IL and Lithium Salt. *Cells* **2020**, *3*, 84. [CrossRef]
39. Fojtášková, J.; Koutník, I.; Vráblová, M.; Sezimová, H.; Maxa, M.; Obalová, L.; Pánek, P. Antibacterial, Antifungal and Ecotoxic Effects of Ammonium and Imidazolium Ionic Liquids Synthesized in Microwaves. *Molecules* **2020**, *25*, 5181. [CrossRef]
40. Dupont, J. From Molten Salts to Ionic Liquids: A "Nano" Journey. *Acc. Chem. Res.* **2011**, *44*, 1223–1231. [CrossRef]
41. Kar, M.; Plechkova, N.V.; Seddon, K.R.; Pringle, J.M.; Macfarlane, D.R. Ionic Liquids—Further Progress on the Fundamental Issues. *Aust. J. Chem.* **2019**, *72*, 3. [CrossRef]
42. Mano, B.; Jesus, F.; Gonçalves, F.J.M.; Ventura, S.P.M.; Pereira, J.L. Applicability of heuristic rules defining structure–ecotoxicity relationships of ionic liquids: An integrative assessment using species sensitivity distributions (SSD). *Green Chem.* **2020**, *22*, 6176–6186. [CrossRef]
43. Pernak, J.; Łęgosz, B.; Walkiewicz, F.; Klejdysz, T.; Borkowski, A.; Chrzanowski, Ł. Ammonium ionic liquids with anions of natural origin. *RSC Adv.* **2015**, *5*, 65471–65480. [CrossRef]

44. Mezzetta, A.; Łuczak, J.; Woch, J.; Chiappe, C.; Nowicki, J.; Guazzelli, L. Surface active fatty acid ILs: Influence of the hydrophobic tail and/or the imidazolium hydroxyl functionalization on aggregates formation. *J. Mol. Liq.* **2019**, *289*, 111155. [CrossRef]
45. Adamová, G.; Gardas, R.; Rebelo, L.P.; Robertson, A.J.; Seddon, K.R. Alkyltrioctylphosphonium chloride ionic liquids: Synthesis and physicochemical properties. *Dalton Trans.* **2011**, *40*, 12750–12764. [CrossRef]
46. Adamová, G.; Gardas, R.L.; Nieuwenhuyzen, M.; Puga, A.V.; Rebelo, L.P.N.; Robertson, A.J.; Seddon, K.R. Alkyltributylphosphonium chloride ionic liquids: Synthesis, physicochemical properties and crystal structure. *Dalton Trans.* **2012**, *41*, 8316. [CrossRef] [PubMed]
47. Firmansyah, M.L.; Kubota, F.; Yoshida, W.; Goto, M. Application of a Novel Phosphonium-Based Ionic Liquid to the Separation of Platinum Group Metals from Automobile Catalyst Leach Liquor. *Ind. Eng. Chem. Res.* **2019**, *58*, 3845–3852. [CrossRef]
48. Xun, S.; Ti, Q.; Wu, L.; He, M.; Wang, C.; Chen, L.; Yang, W.; Zhu, L.; Zhu, W.; Li, H. Few Layer g-C3N4 Dispersed Quaternary Phosphonium Ionic Liquid for Highly Efficient Catalytic Oxidative Desulfurization of Fuel. *Energy Fuels* **2020**, *34*, 12379–12387. [CrossRef]
49. Sardar, S.; Mumtaz, A.; Jabeen, E.; Taneez, M.; Wilfred, C.D.; Maqsood, A. Efficient CO2 sorption in phosphonium-based organic salts. *J. Mol. Liq.* **2020**, *318*, 114044. [CrossRef]
50. Goyal, M.; Kumar, S.; Verma, C.; Bahadur, I.; Ebenso, E.E.; Lgaz, H.; Chung, I.-M. Interfacial adsorption behavior of quaternary phosphonium based ionic liquids on metal-electrolyte interface: Electrochemical, surface characterization and computational approaches. *J. Mol. Liq.* **2020**, *298*, 111995. [CrossRef]
51. Ermolaev, V.; Miluykov, V.; Rizvanov, I.; Krivolapov, D.; Zvereva, E.V.; Katsyuba, S.; Sinyashin, O.; Schmutzler, R. Phosphonium ionic liquids based on bulky phosphines: Synthesis, structure and properties. *Dalton Trans.* **2010**, *39*, 5564–5571. [CrossRef] [PubMed]
52. Littke, A.F.; Fu, G.C. Palladium-Catalyzed Coupling Reactions of Aryl Chlorides. *Angew. Chem. Int. Ed.* **2002**, *41*, 4176–4211. [CrossRef]
53. Fleckenstein, C.A.; Plenio, H. Sterically demanding trialkylphosphines for palladium-catalyzed cross coupling reactions—alternatives to PtBu3. *Chem. Soc. Rev.* **2009**, *39*, 694–711. [CrossRef] [PubMed]
54. Arkhipova, D.M.; Ermolaev, V.V.; Miluykov, V.A.; Gubaidullin, A.T.; Islamov, D.R.; Kataeva, O.N.; Ananikov, V.P. Sterically Hindered Phosphonium Salts: Structure, Properties and Palladium Nanoparticle Stabilization. *Nanomaterials* **2020**, *10*, 2457. [CrossRef]
55. Bruker. *APEX-III*; Bruker AXS Inc.: Madison, WI, USA, 2019.
56. Krause, L.; Herbst-Irmer, R.; Sheldrick, G.M.; Stalke, D. Comparison of silver and molybdenum microfocus X-ray sources for single-crystal structure determination. *J. Appl. Crystallogr.* **2015**, *48*, 3–10. [CrossRef]
57. *CrysAlisPro*; Version 1.171.41.106a; Rigaku Oxford Diffraction: Austin, TX, USA, 2021.
58. Sheldrick, G.M. SHELXT—Integrated space-group and crystal-structure determination. *Acta Crystallogr. Sect. A Found. Adv.* **2015**, *71*, 3–8. [CrossRef]
59. Sheldrick, G.M. Crystal structure refinement with SHELXL. *Acta Crystallogr. Sect. C Struct. Chem.* **2015**, *71*, 3–8. [CrossRef]
60. Dolomanov, O.V.; Bourhis, L.J.; Gildea, R.J.; Howard, J.A.K.; Puschmann, H. OLEX2: A complete structure solution, refinement and analysis program. *J. Appl. Crystallogr.* **2009**, *42*, 339–341. [CrossRef]
61. Hoffmann, H.; Schellenbeck, P. Notiz über die Darstellung von Tri-tert.-butylphosphin. *Eur. J. Inorg. Chem.* **1967**, *100*, 692–693. [CrossRef]
62. Al-Otaibi, J.S.; Gogary, T.M.E.; El-Demerdash, S.H. Umbrella inversion and structure of phosphorus-containing compounds: A quantum chemical study. *J. Theor. Comput. Chem.* **2018**, *17*, 1850042. [CrossRef]
63. Holbrey, J.D.; Rogers, R.D.; Mantz, R.A.; Trulove, P.C.; Cocalia, V.A.; Visser, A.E.; Anderson, J.L.; Anthony, J.L.; Brennecke, J.F.; Maginn, E.J.; et al. Physicochemical Properties. In *Ionic Liquids in Synthesis*, 2nd ed.; Wasserscheid, P., Welton, T., Eds.; Wiley-VCH: Weinheim, Germany, 2008; pp. 57–174.
64. Banerjee, A.; Scott, R.W.J. Optimization of transition metal nanoparticle-phosphonium ionic liquid composite catalytic systems for deep hydrogenation and hydrodeoxygenation reactions. *Green Chem.* **2014**, *17*, 1597–1604. [CrossRef]
65. Chacon, G.; Dupont, J. Arene Hydrogenation by Metal Nanoparticles in Ionic Liquids. *ChemCatChem* **2019**, *11*, 333–341. [CrossRef]
66. Chen, J.; Xie, F.; Li, X.; Chen, L. Ionic liquids for the preparation of biopolymer materials for drug/gene delivery: A review. *Green Chem.* **2018**, *20*, 4169–4200. [CrossRef]
67. Hemmati, M.; Rajabi, M.; Asghari, A. Magnetic nanoparticle based solid-phase extraction of heavy metal ions: A review on recent advances. *Microchim. Acta* **2018**, *185*, 160. [CrossRef]
68. Yi, L.; Wu, W.; Li, T. Crystalline Nanoparticles. In *Pharmaceutical Crystals: Science and Engineering*, 1st ed.; Li, T., Mattei, A., Eds.; John Wiley & Sons, Inc.: Hoboken, NJ, USA, 2019; Volume 11, pp. 463–503.
69. Saldan, I.; Semenyuk, Y.; Marchuk, I.; Reshetnyak, O. Chemical synthesis and application of palladium nanoparticles. *J. Mater. Sci.* **2015**, *50*, 2337–2354. [CrossRef]
70. Zhang, B.; Yan, N. Towards Rational Design of Nanoparticle Catalysis in Ionic Liquids. *Catalysts* **2013**, *3*, 543–562. [CrossRef]
71. Yan, N.; Yuan, Y.; Dyson, P.J. Nanometallic chemistry: Deciphering nanoparticle catalysis from the perspective of organometallic chemistry and homogeneous catalysis. *Dalton Trans.* **2013**, *42*, 13294–13304. [CrossRef]
72. Nützenadel, C.; Züttel, A.; Chartouni, D.; Schmid, G.; Schlapbach, L. Critical size and surface effect of the hydrogen interaction of palladium clusters. *Eur. Phys. J. D* **2000**, *8*, 245–250. [CrossRef]

73. Eremin, D.; Ananikov, V.P. Understanding active species in catalytic transformations: From molecular catalysis to nanoparticles, leaching, "Cocktails" of catalysts and dynamic systems. *Co-Ord. Chem. Rev.* **2017**, *346*, 2–19. [CrossRef]
74. Gnad, C.; Abram, A.; Urstoeger, A.; Weigl, F.; Schuster, M.; Köhler, K. Leaching Mechanism of Different Palladium Surface Species in Heck Reactions of Aryl Bromides and Chlorides. *ACS Catal.* **2020**, *10*, 6030–6041. [CrossRef]
75. Schlögl, R. Heterogeneous Catalysis. *Angew. Chem. Int. Ed.* **2015**, *54*, 3465–3520. [CrossRef] [PubMed]
76. Azov, V.A.; Egorova, K.; Seitkalieva, M.M.; Kashin, A.; Ananikov, V.P. "Solvent-in-salt" systems for design of new materials in chemistry, biology and energy research. *Chem. Soc. Rev.* **2018**, *47*, 1250–1284. [CrossRef] [PubMed]